

1 STANDARD MODEL IS BEST MODEL (WORKING TITLE)

2 William Kennedy DiClemente

3 A DISSERTATION

4 in

5 Physics and Astronomy

6 Presented to the Faculties of The University of Pennsylvania

7 in Partial Fulfillment of the Requirements for the Degree of Doctor of Philosophy

8 2018 Last compiled: December 27, 2018

9

10 I. Joseph Kroll, Professor, Physics
11 Supervisor of Dissertation

12

13 Joshua Klein, Professor, Physics
14 Graduate Group Chairperson

15 Dissertation Committee

16 (Committee Prof. 1), Professor, Physics

17 (Committee Prof. 2), Associate Professor, Physics

18 (Committee Prof. 3), Professor, Physics

19 (Committee Prof. 4), Professor, Physics

20 I. Joseph Kroll, Professor, Physics

21

STANDARD MODEL IS BEST MODEL (WORKING TITLE)

22

COPYRIGHT

23

2018

24

William Kennedy DiClemente

25

All rights reserved.

Acknowledgements

27 I'd like to thanks the Ghosts of Penn Students Past for providing me with such an amazing thesis
28 template.

29

ABSTRACT

30

STANDARD MODEL IS BEST MODEL (WORKING TITLE)

31

William Kennedy DiClemente

32

J. Kroll

33

This is the abstract text.

Contents

35	Acknowledgements	iii
36	Abstract	iv
37	Contents	v
38	List of Tables	viii
39	List of Figures	ix
40	Preface	x
41	1 Introduction	1
42	2 Theoretical Framework	2
43	2.1 Introduction to the Standard Model	2
44	2.2 Electroweak Mixing and the Higgs Field	2
45	3 LHC and the ATLAS Detector	3
46	3.1 The Large Hadron Collider	3
47	3.2 The ATLAS Detector	3
48	3.2.1 The Inner Detector	3
49	3.2.1.1 Pixel Detector	3
50	3.2.1.2 Semiconductor Tracker	3
51	3.2.1.3 Transition Radiation Tracker	3
52	3.2.2 The Calorimeters	4

53	3.2.2.1	Liquid Argon Calorimeters	4
54	3.2.2.2	Tile Calorimeters	4
55	4	Alignment of the ATLAS Inner Detector	5
56	4.1	Effects of Misalignment	5
57	4.2	The Alignment Method	5
58	4.3	Momentum Bias Corrections	5
59	4.4	Alignment of the IBL	6
60	4.5	Alignment Monitoring	6
61	5	WZ production @ $\sqrt{s} = 13$ TeV	7
62	5.1	Theoretical motivation	7
63	5.2	Signal definition	7
64	5.3	Background estimations	7
65	5.4	Cross section measurement	7
66	6	Same-sign WW @ $\sqrt{s} = 13$ TeV	8
67	6.1	Theoretical motivation	8
68	6.2	Signal definition	8
69	6.3	Background estimations	8
70	6.4	Cross section measurement	8
71	7	Prospects for same-sign WW at the High Luminosity LHC	9
72	7.1	Theoretical motivation	9
73	7.2	Signal definition	9
74	7.2.1	Sensitivity to longitudinal polarization	10
75	7.3	Background estimations	10
76	7.4	Selection optimization	10
77	7.4.1	Random grid search algorithm	10
78	7.4.2	Inputs to the optimization	12
79	7.4.3	Results of the optimization	12
80	7.5	Cross section measurement	12
81	8	Conclusion	16

82	Bibliography
----	---------------------

17

List of Tables

List of Figures

85	3.1	General cut-away view of the ATLAS detector.	4
86	7.1	A visual representation of a rectangular grid search algorithm. The signal events are the	
87		blue triangles, and the red circles are the background events. TODO: replace with own	
88		figure	11
89	7.2	A visual representation of a random grid search algorithm. The signal events are the	
90		blue triangles, and the red circles are the background events. TODO: replace with own	
91		figure	11
92	7.3	Leading lepton p_T distribution. The default and optimized cuts are represented by the	
93		red and green dashed lines, respectively. The $W^\pm W^\pm jj$ EWK signal (black points) is	
94		normalized to the same area as the sum of the backgrounds (colored histogram).	13
95	7.4	Dilepton invariant mass distribution. The default and optimized cuts are represented by	
96		the red and green dashed lines, respectively. The $W^\pm W^\pm jj$ EWK signal (black points)	
97		is normalized to the same area as the sum of the backgrounds (colored histogram).	13
98	7.5	Leading (top) and subleading (bottom) jet p_T distributions. The default and optimized	
99		cuts are represented by the red and green dashed lines, respectively. The $W^\pm W^\pm jj$ EWK	
100		signal (black points) is normalized to the same area as the sum of the backgrounds	
101		(colored histogram).	14
102	7.6	Dijet invariant mass distribution. The default and optimized cuts are represented by the	
103		red and green dashed lines, respectively. The $W^\pm W^\pm jj$ EWK signal (black points) is	
104		normalized to the same area as the sum of the backgrounds (colored histogram).	15
105	7.7	Lepton-jet centrality distribution. The default and optimized cuts are represented by the	
106		red and green dashed lines, respectively. The $W^\pm W^\pm jj$ EWK signal (black points) is	
107		normalized to the same area as the sum of the backgrounds (colored histogram).	15

Preface

109 This is the preface. It's optional, but it's nice to give some context for the reader and stuff.

Will K. DiClemente
Philadelphia, February 2019

111

CHAPTER 1

112

Introduction

113 The Standard Model (SM)¹ has been remarkably successful...

¹Here's a footnote.

CHAPTER 2

Theoretical Framework

(Some example introductory text for this chapter)...

2.1 Introduction to the Standard Model

Modern particle physics is generally interpreted in terms of the Standard Model (SM). This is a quantum field theory which encapsulates our understanding of the electromagnetic, weak, and strong interactions...

2.2 Electroweak Mixing and the Higgs Field

When the theory of the electroweak interaction was first developed [1, 2], the W and Z bosons were predicted to be massless (a typical mass term in the Lagrangian would violate the $SU(2)$ symmetry). However, these were experimentally observed to have masses...

CHAPTER 3

LHC and the ATLAS Detector

3.1 The Large Hadron Collider

The Large Hadron Collider (LHC) [3] is...

3.2 The ATLAS Detector

ATLAS is a general-purpose particle detector...

3.2.1 The Inner Detector

The Inner Detector serves the primary purpose of measuring the trajectories of charged particles...

3.2.1.1 Pixel Detector

The Pixel detector consists of four cylindrical barrel layers and three disk-shaped endcap layers...

3.2.1.2 Semiconductor Tracker

The Semiconductor Tracker uses the same basic technology as the Pixels, but the fundamental unit of silicon is a larger “strip”...

3.2.1.3 Transition Radiation Tracker

The Transition Radiation Tracker is the outermost component of the ID...

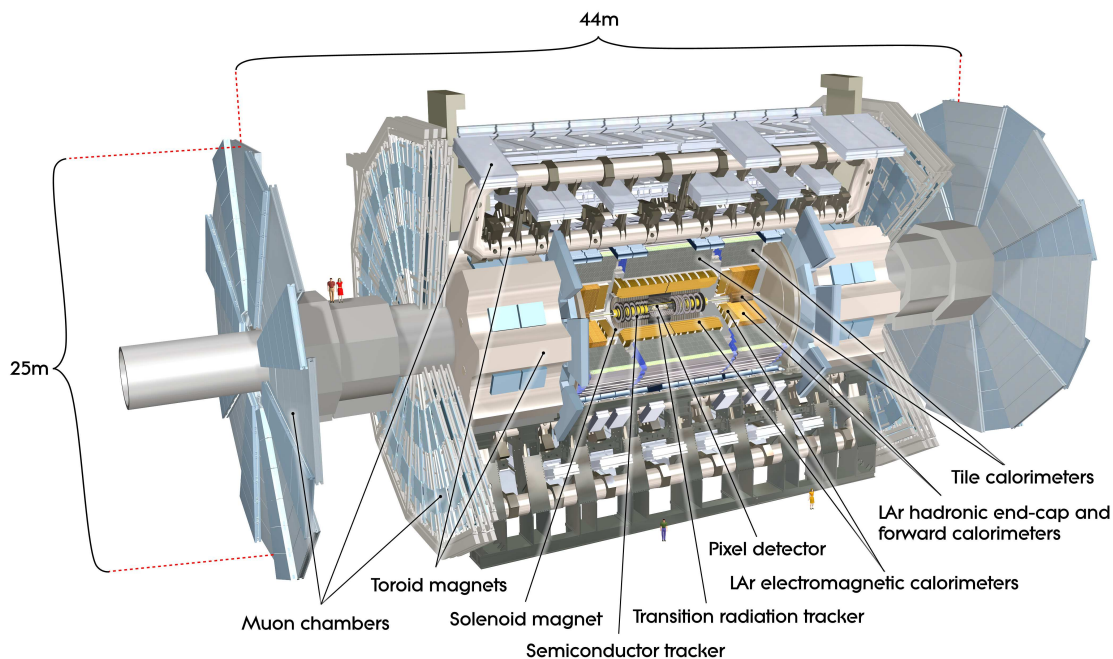


Figure 3.1: General cut-away view of the ATLAS detector [4].

140 3.2.2 The Calorimeters

141 ATLAS includes two types of calorimeter system for measuring electromagnetic and hadronic show-
 142 ers. These are the Liquid Argon (LAr) calorimeters and the Tile calorimeters. Together, these cover
 143 the region with $|\eta| < 4.9$...

144 3.2.2.1 Liquid Argon Calorimeters

145 The Liquid Argon system consists of...

146 3.2.2.2 Tile Calorimeters

147 The Tile calorimeter provides coverage for hadronic showers...

Alignment of the ATLAS Inner Detector

150 In order for the subdetectors of the ID to operate at their designed precisions, it is essential that
151 the locations of the sensors be known as precisely as possible. Differences between the expected and
152 actual positions of a sensor can result in displaced particle hits and degrade track reconstruction
153 quality. These misalignments can occur for any number of reasons, including but not limited to
154 elements shifting during maintenance periods or cycles in ATLAS's magnetic field, or simply small
155 movements during normal detector operations. Since it is not practical to physically realign hundreds
156 of thousands of detector elements to μm precision by hand, an iterative track-based alignment
157 algorithm is used to determine the physical positions and orientations of these elements [5]. The
158 effects of misalignments and the steps taken to correct and monitor them are detailed in this chapter.

159 4.1 Effects of Misalignment

160 Hello world!

161 4.2 The Alignment Method

162 Hello world!

163 4.3 Momentum Bias Corrections

164 Hello world!

165 **4.4 Alignment of the IBL**

166 Hello world!

167 **4.5 Alignment Monitoring**

168 Hello world!

169

CHAPTER 5

170

WZ production @ $\sqrt{s} = 13$ TeV

171 5.1 Theoretical motivation

172 Hello world!

173 5.2 Signal definition

174 Hello world!

175 5.3 Background estimations

176 Hello world!

177 5.4 Cross section measurement

178 Hello world!

179

CHAPTER 6

180

Same-sign WW @ $\sqrt{s} = 13$ TeV

181 6.1 Theoretical motivation

182 Hello world!

183 6.2 Signal definition

184 Hello world!

185 6.3 Background estimations

186 Hello world!

187 6.4 Cross section measurement

188 Hello world!

CHAPTER 7

Prospects for same-sign WW at the High Luminosity LHC

On December 3, 2018, Run 2 of the LHC officially ended, and the collider was shut down to begin the first of two scheduled extended maintenance periods [6]. During these two long shutdowns, the Phase-I and Phase-II upgrades of the LHC and ATLAS will occur in order to prepare for the High-Luminosity LHC (HL-LHC) which is scheduled to begin operation in 2026 [7].

The HL-LHC is planned to run at an instantaneous luminosity of $\mathcal{L} = 5 \times 10^{34} \text{ cm}^{-2}\text{s}^{-1}$ with an average of 140 collisions per beam-crossing. Over the course of operation, the HL-LHC is expected to collect a total integrated luminosity of $\mathcal{L} = 3000 \text{ fb}^{-1}$ by 2035 [8].

These run conditions are much harsher than what ATLAS has experienced so far, and as a result there are several planned upgrades to the detector. Most notably, the entire ID will be replaced with an all-silicon tracker which will extend the coverage from $|\eta| \leq 2.7$ up to $|\eta| \leq 4.0$. This will allow for reconstruction of charged particle tracks which can in turn be matched to clusters in the calorimeters for electron identification or forward jet tagging [9].

TODO: Why are we studying ssww at the HL-LHC

7.1 Theoretical motivation

The theoretical motivation for studying the ssWW process is detailed in Section 6.1.

7.2 Signal definition

Hello world!

7.2.1 Sensitivity to longitudinal polarization

7.3 Background estimations

Hello world!

7.4 Selection optimization

As mentioned earlier, the HL-LHC will feature forward tracking, an increase in center of mass energy, and a higher integrated luminosity. Therefore, this study is an excellent time to see if there are new optimizations to the signal event selection that can improve the signal to background ratio.

7.4.1 Random grid search algorithm

The chosen algorithm for optimizing the event selection is known as the Random Grid Search (RGS) [10]. Consider a simple case of two variables x and y chosen to differentiate the signal from the background. In order to be considered a signal event, a given event would be required to pass a *cut point* $c = \{x > x_c, y > y_c\}$. A simple method to choose the optimal cut point (i.e. the “best” values of the cuts x_c and y_c) would be to construct an $n \times m$ rectangular grid in x and y consisting of points $(x_0, y_0), (x_1, y_1), \dots, (x_n, y_m)$, as in Figure 7.1. One can then choose a cut point $c_k = \{x > x_i, y > y_j\}$ that maximizes the signal significance as measured by a chosen metric. This would be considered a *regular* or *rectangular* grid search.

While effective in principle, this rectangular grid search comes with two major drawbacks:

1. The algorithm does not scale well as the number of variables to be optimized—the dimensionality of the grid—increases. In the case of a square grid with N bins per variable v , the number of cut points to be evaluated grows as N^v .
2. Signal and background samples are rarely evenly distributed over the entire grid, resulting in many cut points being sub-optimal and evaluating them would be a waste of computing resources.

To combat these limitations, the RGS algorithm constructs a grid of cut points directly from the signal sample itself. In the two-dimensional example, this means that the variables x_i and y_j making up the cut point $c_k = \{x > x_i, y > y_j\}$ take their values directly from a given signal event. This has the benefit of creating a *random grid* of cut points that is by construction biased towards

regions of high signal concentration. This reduces the need for exponentially increasing numbers of cut points while ensuring that computing resources are not wasted in regions with few to no signal events. An example of the the two-dimensional random grid is shown in Figure 7.2.

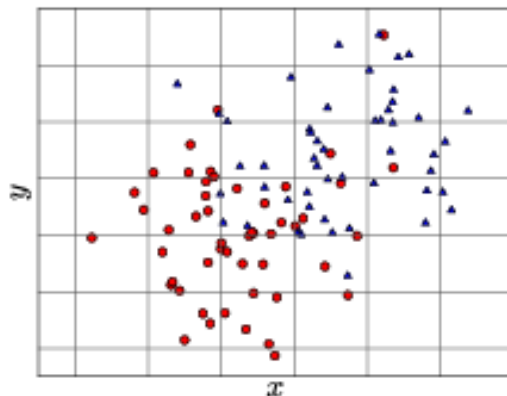


Figure 7.1: A visual representation of a rectangular grid search algorithm. The signal events are the blue triangles, and the red circles are the background events. **TODO: replace with own figure**

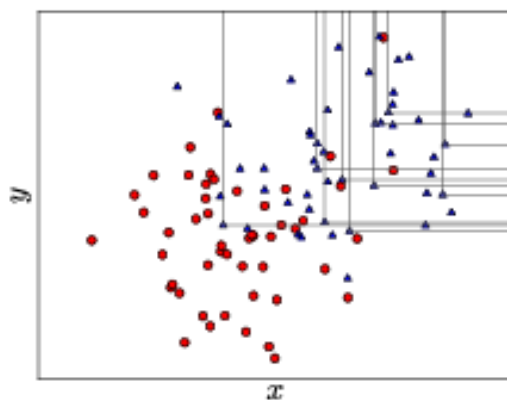


Figure 7.2: A visual representation of a random grid search algorithm. The signal events are the blue triangles, and the red circles are the background events. **TODO: replace with own figure**

Once the random grid of cut points is constructed, the optimal cut point can be chosen using whatever metric the analyzer chooses, such as signal to background ratio. For the purpose of the $W^\pm W^\pm jj$ upgrade study, the optimal cut point is the one that mazimizes the signal significance Z

242 defined as in Equation 7.1 [11].

$$Z = \sqrt{2 \left[(s+b) \ln \left(\frac{s+b}{b_0} \right) + b_0 - s - b \right] + \frac{(b-b_0)^2}{\sigma_b^2}} \quad (7.1)$$

243 where s and b are the number of signal and background events, respectively, σ_b is the total uncertainty
244 on the background, and b_0 is defined as:

$$b_0 = \frac{1}{2} \left(b - \sigma_b^2 + \sqrt{(b - \sigma_b^2)^2 + 4(s+b)\sigma_b^2} \right) \quad (7.2)$$

245 In the case where the background is known precisely (i.e. $\sigma_b = 0$), Equation 7.1 simplifies to

$$Z = \sqrt{2 \left(b \left[(1 + s/b) \ln(1 + s/b) - s/b \right] \right)} \quad (7.3)$$

246 which further reduces to the familiar $Z = s/\sqrt{b}$ for the case when $s \ll b$.

247 7.4.2 Inputs to the optimization

248 The RGS algorithm was trained on the sample of LL-polarized $W^\pm W^\pm jj$ events, and the TX-
249 polarized sample was treated as a background for the purpose of the optimization even though it
250 is a subset of the $W^\pm W^\pm jj$ electroweak signal in order to enhance the longitudinal polarization as
251 much as possible.

252 The random grid was constructed from nearly 40,000 LL signal events and

253 The variables chosen for optimization are:

- 254 • Leading lepton p_T
- 255 • Dilepton invariant mass (m_{ll})
- 256 • Leading jet p_T
- 257 • Subleading jet p_T
- 258 • Dijet invariant mass (m_{jj})
- 259 • Lepton-jet centrality (ζ)

260 7.4.3 Results of the optimization

261 7.5 Cross section measurement

262 Hello world!

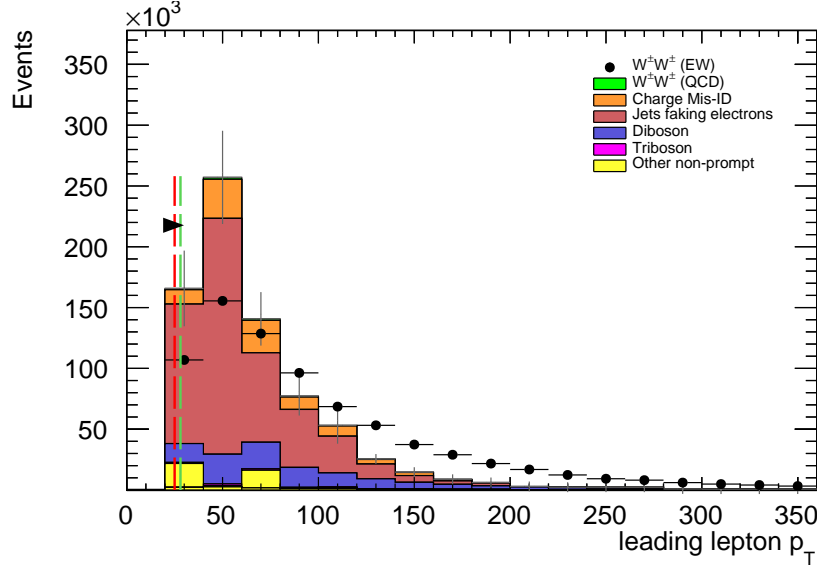


Figure 7.3: Leading lepton p_T distribution. The default and optimized cuts are represented by the red and green dashed lines, respectively. The $W^\pm W^\pm jj$ EWK signal (black points) is normalized to the same area as the sum of the backgrounds (colored histogram).

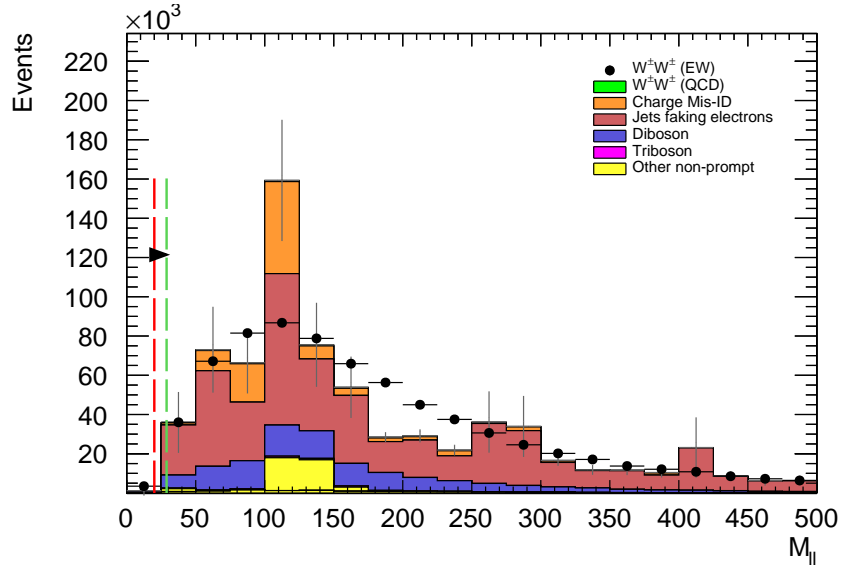


Figure 7.4: Dilepton invariant mass distribution. The default and optimized cuts are represented by the red and green dashed lines, respectively. The $W^\pm W^\pm jj$ EWK signal (black points) is normalized to the same area as the sum of the backgrounds (colored histogram).

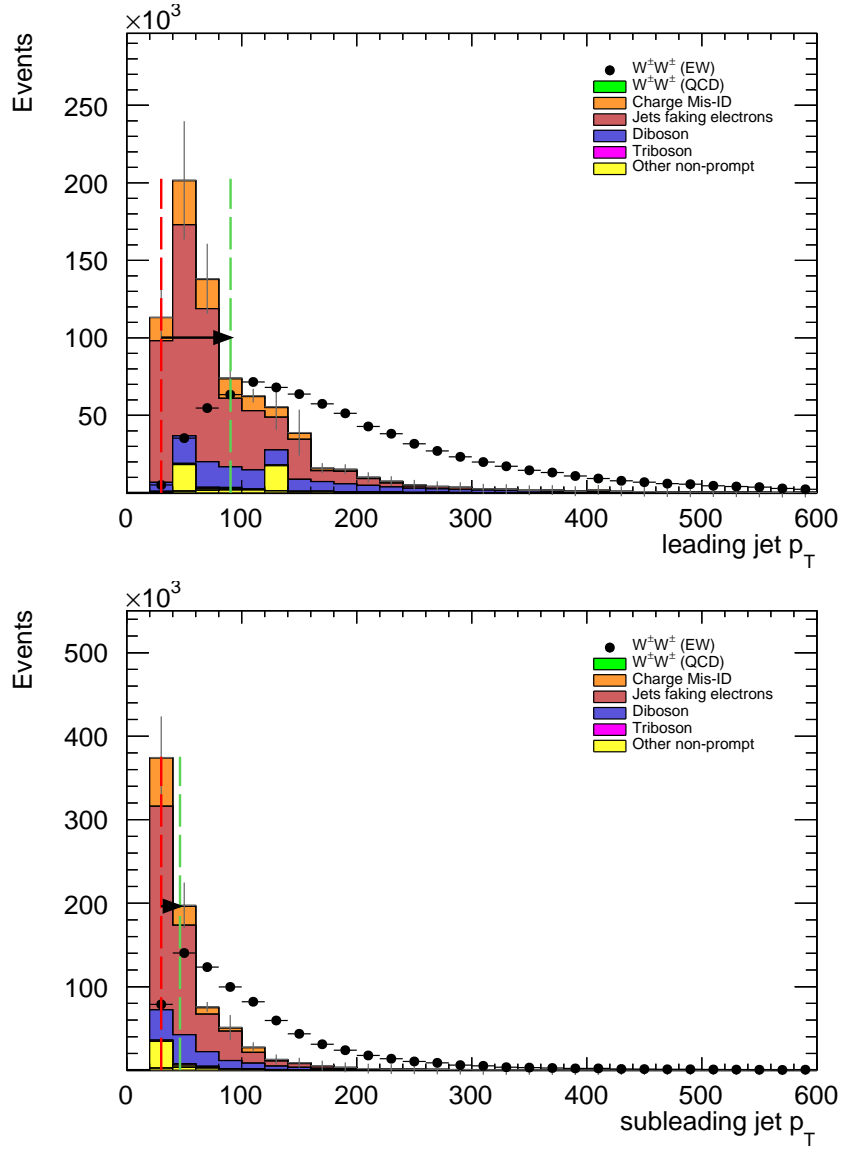


Figure 7.5: Leading (top) and subleading (bottom) jet p_T distributions. The default and optimized cuts are represented by the red and green dashed lines, respectively. The $W^\pm W^\pm jj$ EWK signal (black points) is normalized to the same area as the sum of the backgrounds (colored histogram).

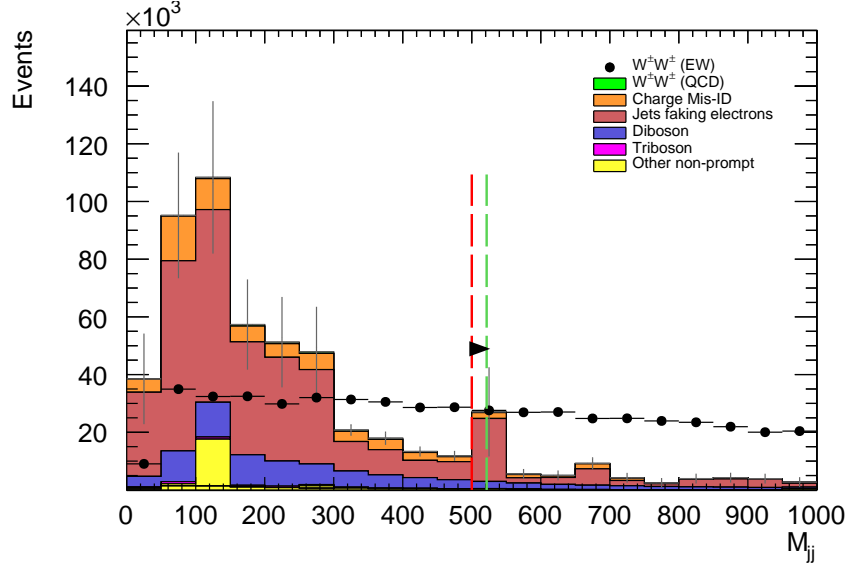


Figure 7.6: Dijet invariant mass distribution. The default and optimized cuts are represented by the red and green dashed lines, respectively. The $W^\pm W^\pm jj$ EWK signal (black points) is normalized to the same area as the sum of the backgrounds (colored histogram).

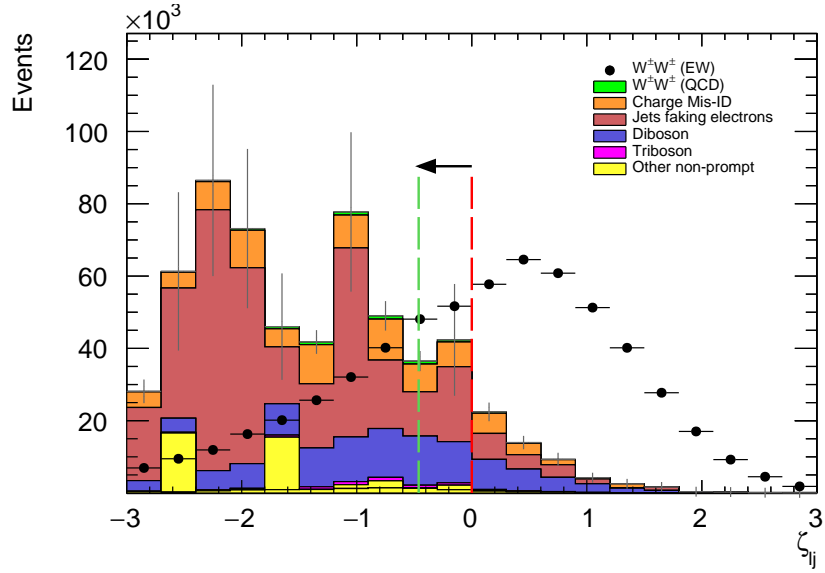


Figure 7.7: Lepton-jet centrality distribution. The default and optimized cuts are represented by the red and green dashed lines, respectively. The $W^\pm W^\pm jj$ EWK signal (black points) is normalized to the same area as the sum of the backgrounds (colored histogram).

263

CHAPTER 8

264

Conclusion

265 Here’s where you wrap it up.

266 **Looking Ahead**

267

268 Here’s an example of how to have an “informal subsection”.

Bibliography

- [1] S. L. Glashow, *The Renormalizability of Vector Meson Interactions*, *Nucl. Phys.* **10** (1959) 107–117. 2.2
- [2] A. Salam and J. C. Ward, *Weak and Electromagnetic Interactions*, *Nuovo Cimento* **11** (1959) 568–577. 2.2
- [3] L. R. Evans and P. Bryant, *LHC Machine*, *JINST* **3** (2008) S08001.
<https://cds.cern.ch/record/1129806>. This report is an abridged version of the LHC Design Report (CERN-2004-003). 3.1
- [4] ATLAS Collaboration, *The ATLAS Experiment at the CERN Large Hadron Collider*, *JINST* **3** (2008) S08003. 3.1
- [5] ATLAS Collaboration Collaboration, *Alignment of the ATLAS Inner Detector Tracking System with 2010 LHC proton-proton collisions at $\sqrt{s} = 7$ TeV*, Tech. Rep. ATLAS-CONF-2011-012, CERN, Geneva, Mar, 2011.
<https://cds.cern.ch/record/1334582>. 4
- [6] R. Steerenberg, *LHC Report: Another run is over and LS2 has just begun...*,
<https://home.cern/news/news/accelerators/lhc-report-another-run-over-and-ls2-has-just-begun>, 2018. Accessed: 2018-12-14. 7
- [7] *Letter of Intent for the Phase-I Upgrade of the ATLAS Experiment*, Tech. Rep. CERN-LHCC-2011-012. LHCC-I-020, CERN, Geneva, Nov, 2011.
<http://cds.cern.ch/record/1402470>. 7
- [8] G. Apollinari, I. Bjar Alonso, O. Brning, M. Lamont, and L. Rossi, *High-Luminosity Large Hadron Collider (HL-LHC): Preliminary Design Report*. CERN Yellow Reports: Monographs. CERN, Geneva, 2015. <https://cds.cern.ch/record/2116337>. 7
- [9] ATLAS Collaboration Collaboration, ATLAS Collaboration, *ATLAS Phase-II Upgrade Scoping Document*, Cern-lhcc-2015-020, Geneva, Sep, 2015.
<http://cds.cern.ch/record/2055248>. 7
- [10] P. C. Bhat, H. B. Prosper, S. Sekmen, and C. Stewart, *Optimizing Event Selection with the Random Grid Search*, *Comput. Phys. Commun.* **228** (2018) 245–257, [arXiv:1706.09907](https://arxiv.org/abs/1706.09907) [hep-ph]. 7.4.1

- 298 [11] G. Cowan, K. Cranmer, E. Gross, and O. Vitells, *Asymptotic formulae for likelihood-based*
299 *tests of new physics*, [Eur. Phys. J. C71 \(2011\) 1554](#), [arXiv:1007.1727 \[physics.data-an\]](#).
300 [Erratum: Eur. Phys. J.C73,2501(2013)]. [7.4.1](#)